Instabilities in Lagrangian Tracking of Bubbles and Particles in Two-Phase Flow

M. F. Göz and M. Sommerfeld
Institut für Mechanische Verfahrenstechnik, Fachbereich Ingenieurwissenschaften, Martin-Luther-Universität Halle-Wittenberg, D-06099 Halle (Saale), Germany

S. Laín
Fluid Mechanics Research Group, Universidad Autónoma de Occidente (UAO), Cali, Colombia

DOI 10.1002/aic.10670
Published online September 29, 2005 in Wiley InterScience (www.interscience.wiley.com).

One way to model and simulate the dispersed phase in a two-phase flow is to track the discrete elements through a fluctuating fluid field by solving their equations of motion. This approach is called Lagrangian. In this frame, it has been shown previously that widely used discretization methods for integrating the particle equation of motion in bubbly flows may lead to artificial instabilities and, eventually, yield spurious oscillations and chaotic behavior by period-doubling bifurcations. This study extends these previous investigations to consider dispersed two-phase flow laden with solid particles, which can be heavier or lighter than the fluid in which they are immersed. The main result is that the numerical techniques applied to integrate the particle or bubble equation of motion are stable in the case of heavy particles but must be used very carefully when applied to bubbles or light solid particles in a fluid. During the analysis process, criteria have been established for choosing optimal time steps to simultaneously avoid numerical instabilities and guarantee code efficiency. © 2005 American Institute of Chemical Engineers *AIChE J,* 52: 469–477, 2006

Introduction

Two-phase, or rather, multiphase media are the rule and not the exception both in nature and industrial practice. However, in contrast to single-phase flow, where the equations of motion and thermal properties are well accepted (Navier–Stokes–Fourier equations), the state of the art for multiphase flows is considerably more primitive in that the correct formulation of the governing equations is still subject to debate.

Two-phase flows of dispersed particles, drops, or bubbles in an ambient fluid are modeled mainly in two ways: the Euler–Euler and the Euler–Lagrange approach.[1-4] In the Euler–Euler formulation, the two phases are considered as two interpenetrating and mutually interacting continua; here, appropriate closure relations for the interaction terms and the effective properties of the fluidlike dispersed phase have to be found. For establishing the equations governing the motion of the dispersed elements, two approaches are mainly applied. First, the dispersed phase is considered as a fluid in all respects. This corresponds to the well-known two-fluid description.[5] Second, the noncontinuous phase is viewed as a cloud of material elements, whose behavior is driven by a probability density function (PDF), which depends on the state variables of each element, and responds to a kinetic transport equation similar to the Maxwell–Boltzmann equation. The continuum equations for the dispersed phase are then obtained as the statistical moments of such a PDF-evolution equation.[6,7]

In the Euler–Lagrange approach particles, or rather representatives of particles, are tracked by solving the equation of

Present address of M. F. Göz is Mörikerstr. 16, D-71522 Backnang, Germany.
M. Sommerfeld is also affiliated with Fluid Mechanics Research Group, Universidad Autónoma de Occidente (UAO), Cali, Colombia.
Correspondence concerning this article should be addressed to S. Laín at santiago.lain@gmail.com *or* slain@uao.edu.co.

© 2005 American Institute of Chemical Engineers

motion for a small body immersed in a flow field where, generally, the assumption of point-particles is made. The fluid field is calculated by solving the Navier–Stokes equations, possibly in connection with a turbulence model. The movement of a particle or bubble is obtained by solving Newton's equation containing the forces acting on it. To evaluate these, the instantaneous fluid velocity at the location of the particle is determined as the sum of the local mean fluid velocity and a fluctuating component described, for example, by a Markov process.[8] Within one Eulerian time step several Lagrangian time steps are performed; after calculating the particle movement during one Eulerian time step the fluid velocity is updated, taking account of the source terms generated by the particles. The advantage of the Euler–Lagrange approach is that it can elegantly account for several complex phenomena such as particle or bubble size distributions, particle–wall collisions, coalescence, and breakup, or chemical processes such as vaporization and combustion, all of them very difficult to handle in a pure Eulerian framework.

In the context of the Lagrangian frame the majority of approaches solve the particle motion equation using a Monte Carlo method, which involves tracking a large number of particle trajectories of representative particle samples. By applying such a strategy to the movement of gas bubbles in liquid (air bubbles in a water column), it was previously found[9] that the bubble velocity did not always settle down to a terminal rise velocity as expected, but oscillated sometimes between two, four, or more velocity values. It even appeared to behave erratically in a range of bubble Reynolds numbers. This phenomenon was shown to be caused by the form of the coefficient of the drag force combined with the numerical discretization scheme used for the solution of the bubble equation. Also in the same article, criteria for avoiding such nonphysical oscillations were given for certain numerical integration schemes, that is, a *semianalytical approach*, in which the particle momentum equation is solved analytically over small time steps assuming that the instantaneous fluid velocity and the particle relaxation time are constant,[2] and the simple Euler scheme and the Runge–Kutta methods are of order two and four.

This study reported herein extends the aforementioned analysis to the case of free-falling heavy particles and the rise of light solid particles in a medium at rest. It is shown that the previous numerical integration schemes of the particle motion equation behave robustly in the case of heavy particles but should be used very carefully when applied to light particles rising in a stagnant liquid.

Particle Dynamics

Tracking of the discrete element by the Lagrangian method requires the solution of the "particle" (that is, bubble, droplet, or solid) motion equation. This equation is built using Newton's second law of motion provided all the forces acting on a particle immersed in a flow field are quantified. These forces can be divided into four categories: (1) forces that act on a particle arising from its motion; (2) forces that act on a particle arising from the motion of the surrounding fluid; (3) body forces; and (4) forces that act on any object immersed in a fluid irrespective of either particle or fluid motion. The mathematical expression for the particle motion equation of a spherical particle accounting for all four types of forces is given by[10,11]

$$\underbrace{m_p \frac{d}{dt}\,\boldsymbol{v}}_{\text{Inertia}} = \underbrace{3\pi D_p \mu f(\boldsymbol{u}_f - \boldsymbol{v})}_{\text{Drag}} + \underbrace{K_m \rho D_p^3 \frac{\pi}{6}\frac{d}{dt}[\boldsymbol{u}_f - \boldsymbol{v}]}_{\text{Added Mass}} + \underbrace{K_B D_p^2 \sqrt{\pi\rho\mu}\int_{t_0}^{t}\frac{d}{dt}[\boldsymbol{u}_f - \boldsymbol{v}]\frac{dt'}{\sqrt{t-t'}}}_{\text{Basset}} + \frac{\pi}{8}\underbrace{\rho D_p^3(\nabla\times\boldsymbol{v})\times(\boldsymbol{u}_f - \boldsymbol{v})}_{\text{Magnus}} + \underbrace{m_p\boldsymbol{g}}_{\text{Weight}} - \underbrace{\rho\frac{\pi}{6}D_p^3\boldsymbol{g}}_{\text{Buoyancy}} \quad (1)$$

Here, $\boldsymbol{u}_f$ and $\boldsymbol{v}$ denote the fluid and particle instantaneous velocities, respectively; ρ and ρ_p are the fluid and particle densities; D_p and m_p are the particle diameter and its mass; μ is the fluid viscosity; and $\boldsymbol{g}$ is the constant of gravity. K_m and K_B represent the coupling constants of the added mass and Basset forces. Finally, $f(\boldsymbol{u}_f - \boldsymbol{v})$ is a function of the relative velocity necessary to determine the steady drag force. For a derivation and discussion of Eq. 1 the reader is referred to Maxey and Riley[10] and Magnaudet.[11]

In many applications, such as in the case of dilute flows with spherical dispersed elements, it is possible to simplify Eq. 1 and consider only the drag, gravity–buoyancy forces, and, in the case of bubbles or light particles, the added mass force. Therefore, in the literature the following expression is often found:

$$\frac{d}{dt}\boldsymbol{v} = \frac{1}{\tau_p}(\boldsymbol{u}_f - \boldsymbol{v}) + \left(1 - \frac{\rho}{\rho_p}\right)\boldsymbol{g} + K_m\frac{\rho}{\rho_p}\frac{d}{dt}[\boldsymbol{u}_f - \boldsymbol{v}]$$

$$\tau_p = \frac{4\rho_p D_p^2}{3\mu}\frac{1}{\mathrm{Re}\,C_D(\mathrm{Re})} \qquad \mathrm{Re} = \frac{\rho D_p|\boldsymbol{u}_f - \boldsymbol{v}|}{\mu} \quad (2)$$

where τ_p is the relaxation time of the particle, Re isthe Reynolds number based on the relative velocity, and $C_D(\mathrm{Re})$ is the drag coefficient. The drag coefficient can be analytically derived for small Reynolds numbers only (Stokes regime), and must otherwise be determined experimentally and be verified by direct numerical simulation if possible. There is no single (and especially no simple) formula for the drag coefficient; usually it is described piecewise as a fit to experimental data.[12] On the other hand, for a sphere it is known[11] that $K_m = 1/2$ and for bubbles, whose shape deviates from the spherical one, other correlations are available in the literature.[13]

Before discussing the actual numerical integration behavior of the particle motion equation, we would like remark the following points:

- In principle, Eq. 2 is an equation in $\mathbf{R}^3$, but to illustrate the main facts it is sufficient to restrict the considerations to the one-dimensional version.
- We are interested in the cases of heavy solids settling in a quiescent fluid and bubbles or light solids rising in a stagnant liquid. Therefore, the fluid velocity will be set to zero, $\boldsymbol{u}_f = 0$, so that Eq. 2 is reduced to

$$\frac{d}{dt}v = -v\tau_p^{-1} + \left(1 - \frac{\rho}{\rho_p}\right)g - K_m\frac{\rho}{\rho_p}\frac{d}{dt}v$$

By collecting the particle acceleration on the left-hand side the following expression is obtained:

$$\left(1 + K_m\frac{\rho}{\rho_p}\right)\frac{d}{dt}v = -v\tau_p^{-1} + \left(1 - \frac{\rho}{\rho_p}\right)g$$

and by rescaling the time as $t' = t/(1 + K_m\rho/\rho_p)$ Eq. 2 is finally cast into the form

$$\frac{d}{dt'}v = -v\tau_p^{-1} + \left(1 - \frac{\rho}{\rho_p}\right)g \tag{3}$$

This expression is formally the same as that in the case where the added mass force is omitted (that is, $K_m = 0$), with the only difference of time rescaling. Therefore, in the following, the numerical integration of Eq. 3 will be worked out, understanding that if $K_m \neq 0$ the time step appearing in the subsequent equations and figures has to be divided by $1 + K_m\rho/\rho_p$.

In Eq. 3 the positive axis direction is taken upward, whereas gravity is directed downward. Therefore, in the case of bubbles or light solids, the rising velocities are positive, but in the case of heavy solids the settling velocities will be negative.

Equation 3 is a nonlinear ordinary differential equation. Therefore, releasing a particle from rest, it will move according to the above equation until it reaches a steady state as the time tends to infinity; this terminal velocity is determined by the solution of the fixed-point equation:

$$v_* = \left(1 - \frac{\rho}{\rho_p}\right)g\tau_p(v_*) \tag{4}$$

However, it must be mentioned that this is a common but idealized description of the real situation. In fact, solid particles, and even more so deformable bubbles, do not move steadily but oscillatory (periodic or aperiodic) at sufficiently high Reynolds numbers; in addition, the motion does not stay rectilinear but becomes two- or three-dimensional. This is not accounted for in the experimentally determined drag coefficient, which is obtained by time-averaging the vertical particle movement. Therefore, in principle, Eq. 2 is an equation in $\mathbf{R}^3$, with a matrix τ_p^{-1}, where the components decouple only for particles in rectilinear motion. For our present purpose, however, it is sufficient to restrict consideration to the one-dimensional version and avoid the additional complexity of a set of coupled nonlinear equations needed to describe the movement of nonspherical and/or nonrectilinearly moving particles. It should be clear that the unsteady behavior described below arises from numerical instabilities and has nothing to do with the experimentally observed oscillations.

The following section deals with various standard methods used for the numerical integration of Eq. 3, necessary for the construction of the particle trajectory.

Numerical Integration Schemes for the Particle Motion Equation

Equation 3 is a first-order, nonhomogeneous, nonlinear differential equation that can be numerically integrated. There are several simple, and therefore common, ways to perform this numerical integration, as summarized in the following.

The semianalytical approach

The particle motion Eq. 3 can be solved analytically over small time steps (Δt), during which the particle relaxation time is assumed to be constant. This approach is widely found in the engineering literature.[2-4] Using the variation-of-constant method, the new particle velocity at instant $t + \Delta t$ can be written as

$$v(t + \Delta t) = v(t)\cdot e^{-\Delta t/\tau_p(t)} + g\left(1 - \frac{\rho}{\rho_p}\right)\tau_p(t)\cdot(1 - e^{-\Delta t/\tau_p(t)}) \tag{5}$$

Several conditions on the (variable) time step arise from the full Euler–Lagrange procedure to obtain a good resolution of the flow structure.[14]

The Euler scheme

This is the simplest numerical integration scheme and in our case can be expressed as

$$v(t + \Delta t) = v(t) + \Delta t\left[-\frac{1}{\tau_p}v(t) + \left(1 - \frac{\rho}{\rho_p}\right)g\right] \tag{6}$$

This scheme can be considered as an approximation of order $O(\Delta t)$ to the semianalytical approach, when the time step is kept constant.

The Runge–Kutta scheme

This widely used standard numerical scheme has several versions depending on the order considered. Here, the second and fourth orders will be taken into account. If, for the sake of brevity, the particle motion Eq. 3 is rewritten as

$$\frac{d}{dt}v = f(v) \qquad f(v) = -\frac{1}{\tau_p}v + \left(1 - \frac{\rho}{\rho_p}\right)g \tag{7}$$

then the second-order Runge–Kutta method approximates the particle velocity in $t + \Delta t$ by

$$v(t + \Delta t) = v(t) + \Delta t\cdot f\left\{v(t) + \frac{\Delta t}{2}f[v(t)]\right\} \tag{8}$$

that is, it is a two-step procedure. Similarly, the fourth-order Runge–Kutta method includes four steps:

$$v(t + \Delta t) = v(t) + \frac{k_1(t)}{6} + \frac{k_2(t)}{3} + \frac{k_3(t)}{3} + \frac{k_4(t)}{6} \tag{9}$$

where

$$k_1(t) = \Delta t\cdot f[v(t)] \qquad k_2(t) = \Delta t\cdot f\left[v(t) + \frac{k_1(t)}{2}\right]$$

$$k_3(t) = \Delta t \cdot f\left[v(t) + \frac{k_2(t)}{2} \right] \qquad k_4(t) = \Delta t \cdot f[v(t) + k_3(t)]$$

The next sections are devoted to the separate descriptions of the following cases: bubbles rising in quiescent water, heavy solids falling through a still fluid, and light solids rising in a liquid.

Bubbles Moving in Clean Quiescent Water

In this section, we focus on the case of air bubbles rising in quiescent water. This selection is motivated by the application of Lagrangian tracking to the numerical simulation of bubble column reactors.[14] For an air bubble rising in clean water the drag coefficient C_D may be given as a function of the Reynolds number as follows; a plot of this and a smoothed drag law are presented in Figure 1.

$$C_D = \begin{cases} 16\ \mathrm{Re}^{-1} & \mathrm{Re} < 1.5 \text{ (regime 1)} \\ 14.9\ \mathrm{Re}^{-0.78} & 1.5 < \mathrm{Re} < 80 \text{ (regime 2)} \\ 48\ \mathrm{Re}^{-1}(1 - 2.21\ \mathrm{Re}^{-0.5}) & 80 < \mathrm{Re} < 700 \text{ (regime 3)} \\ 1.86 \cdot 10^{-15}\mathrm{Re}^{4.756} & 700 < \mathrm{Re} < 1530 \text{ (regime 4)} \\ 2.61 & 1530 < \mathrm{Re} \text{ (regime 5)} \end{cases} \tag{10}$$

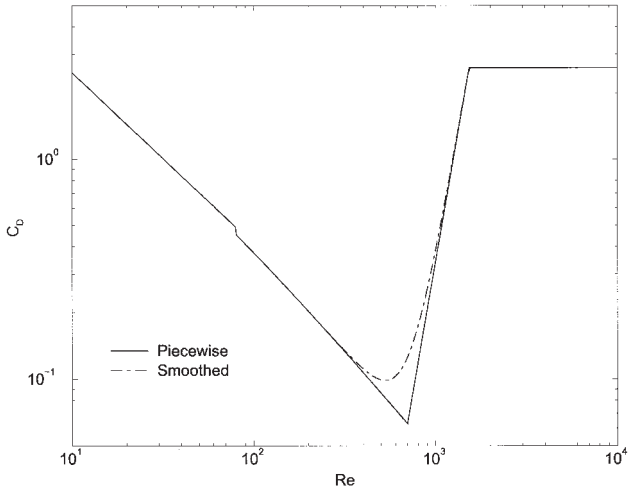

Figure 1. Discontinuous and partially smoothed drag coefficient C_D for bubbles.

Then it is possible to write down the expression for the terminal velocity in dependency on the bubble (equivalent) diameter using the fixed-point Eq. 4:

$$v_* = \begin{cases} 8.06 \cdot 10^5 D_p^2 & D_p < 0.12 \text{ mm (regime 1)} \\ 6.10 \cdot 10^3 D_p^{1.459} & 0.12 \text{ mm} < D_p < 0.61 \text{ mm (regime 2)} \\ 2.53 \cdot 10^{-7} D_p^{-1}[2.21 + \sqrt{2.21^2 + 1.06 \cdot 10^{-12} D_p^3}]^2 & 0.61 \text{ mm} < D_p < 1.34 \text{ mm (regime 3)} \\ 1.32 \cdot 10^{-2} D_p^{-0.56} & 1.34 \text{ mm} < D_p < 8.29 \text{ mm (regime 4)} \\ 2.08 D_p^{0.5} & 8.29 \text{ mm} < D_p \text{ (regime 5)} \end{cases} \tag{11}$$

where the units of v_* are determined by the units of D_p. If in Eq. 11 D_p is introduced in meters, v_* is given in m s^{-1}.

It can be easily confirmed that the above fixed points are stable within the frame of the dynamic Eq. 3. Our purpose from now on is to study how the different numerical integration schemes sketched before perform in the case of Eq. 3.

The semianalytical approach

Assuming that the bubble relaxation time τ_p is constant during small time steps, the pure bubble momentum Eq. 3 can be solved analytically, as was previously indicated. Under the simplified conditions considered here, the discrete version of the solution is Eq. 5, which allows building the bubble velocity at subsequent times. The main question is how to determine the time step Δt. In the problem at hand, the relevant timescale is given by the relaxation time of the bubble, τ_p. This restricts Δt to a fraction of the instantaneous value of τ_p. In the literature, this fraction is chosen anywhere between 0.1 and 0.5 "in order to avoid [numerical] instabilities," without further deliberation of this issue. Thus, by adjusting each time step to the instantaneous bubble relaxation time, $\Delta t_n \propto \tau_{pn}$, Eq. 5 induces the map $f: v_n = v(t) \rightarrow v_{n+1} = v(t + \Delta t_n)$ given by

$$v_{n+1} = A_n \cdot v_n + (1 - A_n) \cdot g\left(1 - \frac{\rho}{\rho_p}\right)\tau_{pn} \equiv f(v_n, D_p)$$
$$\tau_{pn} = \tau_p(v_n) \tag{12}$$

with the parameter $A_n = \exp(-\Delta t_n/\tau_{pn}) = \text{const.} \equiv A$. The fixed points of this map coincide with the steady states $v_*(D_p)$ of the differential equation, but in contrast to the continuous case they may become unstable in a moderately high Reynolds number regime corresponding to air bubbles in water of diameter between 1.34 and 8.29 mm. This gives rise to a whole sequence of instabilities connected with repeated period-doubling bifurcations leading eventually to chaotic behavior.

To determine the stability of the fixed points, it is necessary to compute $f'_* = (df/dv)(v_*)$: v_* is stable if $|f'_*| < 1$, unstable if $|f'_*| > 1$, and in the case $|f'_*| = 1$ the fixed point is said to be marginally stable. To this end, it is useful to represent the bubble relaxation time depending on the drag law given in Eq. 10 as

$$\tau_p^{-1} = \frac{3\mu}{4\rho_p D_p^2}\,\mathrm{Re} \cdot C_D(\mathrm{Re}) = \frac{3\mu}{4\rho_p D_p^2}\,\alpha + \beta\,\mathrm{Re}^{\gamma} \tag{13}$$

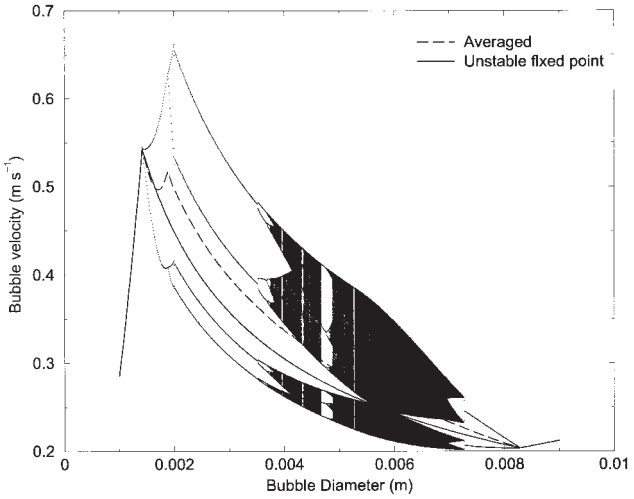

Figure 2. Bifurcation diagram of the map (Eq. 12) for piecewise C_D and A_n fixed to 0.61.

The dashed curve represents the average of all velocities for a given diameter and the solid curve represents the unstable fixed point.

with piecewise defined values of (α, β, γ). Then, the criterion for instability in the different regimes of C_D can be cast in the form

$$\alpha\gamma v_* < \frac{4}{3}\frac{\rho_p g}{\mu}\left(1-\frac{\rho}{\rho_p}\right)\left(\gamma-\frac{1+A_n}{1-A_n}\right)D_p^2 \qquad (14)$$

Now it is straightforward to show that for fixed ratio $\Delta t_n/\tau_n$ the fixed points of regimes 1, 2, 3, and 5 (Eqs. 10 and 11) are always stable, whereas an instability occurs in regime 4 (where $\alpha_4 = 0$) if

$$A < \frac{\gamma_4 - 1}{\gamma_4 + 1} = \frac{4.756}{6.756} \approx 0.704 \qquad (15)$$

This is equivalent to $\Delta t_n/\tau_n > 0.35$, that is, the last ratio should be chosen smaller than 0.35 to ensure stability of the solution method.

If this is not the case, a sequence of instabilities is generated in range 4 of D_p values. First a bifurcation to a solution of period 2 takes place, that is, the solution jumps between two different Reynolds numbers corresponding to two discrete values of bubble velocity. This period 2 solution itself becomes unstable at another critical value of D_p (that is, larger bubble diameter), where a secondary bifurcation to a period 4 solution occurs. This process is repeated over and over again, providing another example of the famous period-doubling route to chaos. It is illustrated in Figure 2, where it is seen that the bands of apparent chaotic behavior (or at least large-n periodic solutions) are interspersed with regions with more regular behavior (small-n periodic solutions), and also that reverse bifurcations occur at large values of D_p until only one—the restabilized "real" fixed-point solution—is left for sufficiently large D_p.

Besides sound methods to avoid these numerical instabilities, one might be tempted to simply "correct" this behavior by averaging over the n values of a solution of period n. This leads to the dashed curve in Figure 2, from which it can be concluded that averaging does not necessarily provide a good approximation to the physical fixed point. The average deviates considerably from the artificially unstable fixed point between bubble diameters of 2 and 8 mm, which are very common sizes for bubbles in industrial applications. The observed behavior depends partially on the form, that is, the nonmonotonicity and nonsmoothness, of the drag coefficient, and can be suppressed to some extent, although not eliminated completely, by smoothing the drag coefficient near the endpoints of the critical Reynolds number interval (regime 4). The most critical point is the right endpoint of regime 4, where the slope of the drag coefficient becomes steepest; this steepness induces most of the bifurcation structure of the iterated map. As an example, choosing a very narrow polynomial, continuously differentiable approximation to the transition between regimes 4 and 5 around Re = 1530 (Figure 1, smoothed drag law) does not significantly change the bifurcation structure, although the bands containing large-n periodic solutions become somewhat smaller.

As an alternative to the method described above, one might use the same semianalytic approach (Eq. 5) but with fixed time step, that is, not adjusted to the relaxation time. The map is like that above but with variable $A_n = \exp(-\Delta t/\tau_n)$. It is also unstable in regime 4, whereas the instability criterion becomes

$$\Delta t > \frac{\tau_p(v_*)}{g\left(1-\frac{\rho}{\rho_p}\right)}\ln\left(\frac{\gamma_4+1}{\gamma_4-1}\right) = 5.57\cdot 10^{-7}D_p^{-0.56} \qquad (16)$$

With $D_p \in (1.34, 8.29)$ mm we obtain $\Delta t_c \in (8.16 \times 10^{-6}, 2.26 \times 10^{-5})$ s for the critical time step, where the smallest critical time step, and thus the main instability, occurs at $D_p = 8.29$ mm. For this case we found behavior that was roughly similar to that described above. The major difference to the first method is that now the time step represents the critical parameter, which has to be chosen quite small to avoid instabilities.

The Euler scheme

Because the Euler method is the $O(\Delta t)$ approximation to the semianalytical approach with fixed time step, it behaves similarly to the last example because it can be written in the form of Eq. 12, with $A_n = 1 - \Delta t/\tau_{pn}$. Thus, the fixed points of this map coincide again with the steady states of the differential equation. However, it is easy to verify that they are more unstable than in the previous scheme. Obviously, the most unstable regime is that of higher values of D_p, and a very small time step has to be chosen to achieve stability in this regime and thus overall stability of the scheme. A further complication arises from the fact that the Euler map can produce nonphysical negative values of v in the range of large D_p when the time step is not small enough.

The Runge–Kutta schemes

Second-order Runge–Kutta. In the simplified situation, Eq. 8 induces the map:

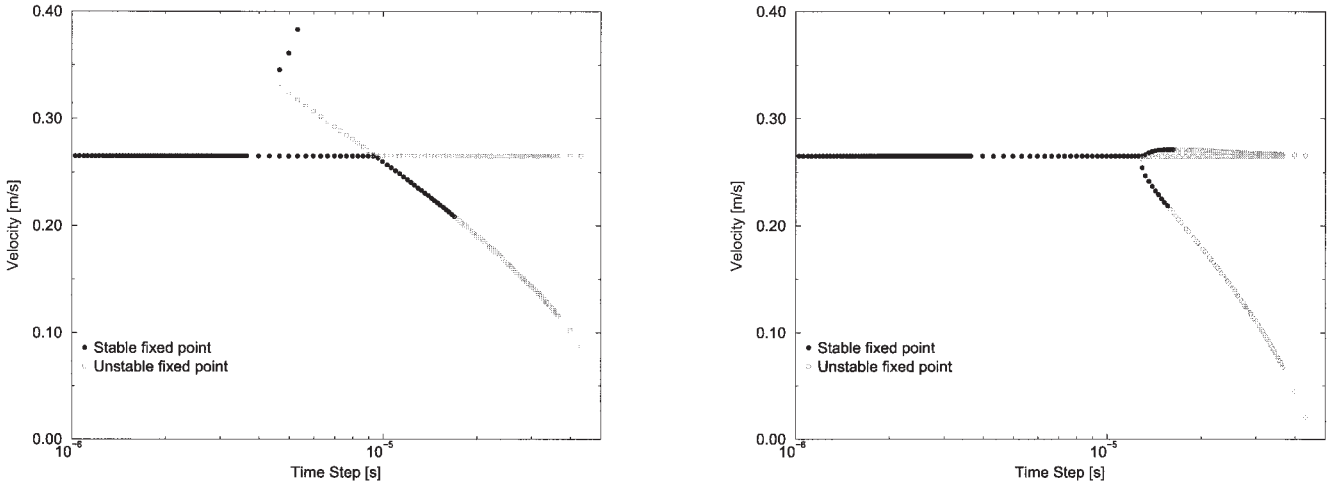

Figure 3. Stability of fixed points vs. time step for the second-order Runge–Kutta (left) and fourth-order Runge–Kutta (right): $D_p = 4.62$ mm.

$$v_{n+1} = v_n + \Delta t \cdot f\left[v_n + \frac{\Delta t}{2} \cdot f(v_n) \right]$$

$$f(v) = -\frac{v}{\tau_p(v)} + \left(1 - \frac{\rho}{\rho_p}\right) g \quad (17)$$

Because this is a two-step method, it can jump between different regimes and thus allow more fixed points than the Euler method (the so-called *ghost* fixed points[15]); this opens the possibility to further instabilities. In addition, in the case of multiple stable fixed points each one has its own basin of attraction, and it depends on the initial condition as to which one will be reached in the time series obtained by iterating the map. The details of such artificial behavior depend, of course, on the magnitude of the time step. This map may be written

$$v_{n+1} = v_n + \Delta t \cdot \left[\left(1 - \frac{\rho}{\rho_p}\right) g - \frac{x_n}{\tau_p(x_n)} \right] \quad (18)$$

with

$$x = x(v) = v\left[1 - \frac{\Delta t}{2\tau_p(v)} \right] + \frac{\Delta t}{2} \left(1 - \frac{\rho}{\rho_p}\right) g \quad (19)$$

Thus the fixed points are given implicitly by $[1 - (\rho/\rho_p)]g = x/\tau_p(x)$, which has a solution $x = X(D_p)$, where $X(D_p)$ denotes the piecewise defined value of v_*as given by Eq. 11. Then the fixed-point equation reads

$$v - \frac{\Delta t \cdot v}{2\tau_p(v)} = X(D_p) - \frac{\Delta t}{2} \left(1 - \frac{\rho}{\rho_p}\right) g \quad (20)$$

Obviously, one solution is always $v_1 = X(D_p)$, which is the only solution for $\Delta t = 0$. However, it can be readily seen that are a number of other solutions depending on the values of D_p and Δt. For a Reynolds number in regime 1, for instance, all solutions are given by

$$v = \frac{X(D_p) - \Delta t \cdot (1 - \rho/\rho_p)\, g/2}{1 - \Delta t \cdot 6\mu/\rho_p D_p^2} \quad (21)$$

provided that D_p is <0.12 mm; for $X(D_p) = X_1(D_p) = [1 - (\rho/\rho_p)]g\rho_p D_p^2/12\mu$ the usual fixed point $v_* = [1 - (\rho/\rho_p)]g\rho_p D_p^2/12\mu$ of regime 1 is obtained. As another example, explicit solutions can be found for v in regime 5; in particular, for

$$X(D_p) = X_5(D_p) = \sqrt{\frac{4}{3} \frac{\rho_p \rho}{\beta_5 \mu^2} \left(1 - \frac{\rho}{\rho_p}\right) g D_p^3}$$

the additional fixed point is given by

$$v_2 = \frac{2}{\Delta t \beta_5} \frac{4\rho_p}{3\rho} D_p - \sqrt{\frac{4}{3} \frac{\rho_p \rho}{\beta_5 \mu^2} \left(1 - \frac{\rho}{\rho_p}\right) g D_p^3} \quad (\beta_5 = 2.61) \quad (22)$$

Other explicit solutions can be calculated only for regime 3. In regimes 2 and 4 we have to consult the implicit function theorem, which gives us bifurcation points $v_b(\Delta t)$ and indicates that additional fixed points exist within certain time-step intervals. Bifurcations off the "true" fixed point of each regime occur when the condition $v_*(2 + \alpha\gamma\Delta t) - 4\Delta t(\gamma + 1)[1 - (\rho/\rho_p)]g\rho_p D_p^2/3\mu = 0$ is fulfilled. An examination of the derivative of the map 17 at a "true" fixed point v_*reveals that it cannot fall below -1, but exceeds $+1$ whenever $f'(v_*) > 0$ or $f'(v_*) < -2/\Delta t$, in which case v_*would be unstable. The first condition is never satisfied here, whereas the second one corresponds to

$$v_*(2 + \alpha\gamma\Delta t) - \Delta t(\gamma + 1) \frac{4}{3} \left(1 - \frac{\rho}{\rho_p}\right) g \frac{\rho_p D_p^2}{\mu} < 0 \quad (23)$$

As an example, Figure 3 (left) provides a sample illustrating the existence and stability of fixed points in dependency on the

time step, for a value of $D_p = 4.62$ mm in the most interesting range. It is possible to see the existence of a stable ghost fixed point in the range $\Delta t \in [4 \times 10^{-6}, 6 \times 10^{-6}]$ s, where the physical fixed point is still stable. This *ghost* fixed point is generated in a saddle-node bifurcation together with an unstable fixed point. Later on, this unstable fixed point collides with the physical fixed point (around $\Delta t \approx 9 \times 10^{-6}$ s) in a transcritical bifurcation. This results in an exchange of stability properties between both points, that is, the unstable fixed point becomes stable and the stable one becomes unstable. Eventually, this last stable fixed point experiences a Hopf or period-doubling bifurcation at $\Delta t \approx 1.5 \times 10^{-5}$ s.

Furthermore, similarly to the Euler map, the second-order Runge–Kutta method will yield nonphysical negative velocity values in range 4 for sufficiently large time steps.

Fourth-order Runge–Kutta. In this case, the map is induced by Eq. 9:

$$v_{n+1} = v_n + k_1/6 + k_2/3 + k_3/3 + k_4/6 \tag{24}$$

with

$$k_1 = hf(v_n) \qquad k_2 = hf\left(v_n + \frac{k_1}{2}\right) \qquad k_3 = hf\left(v_n + \frac{k_2}{2}\right)$$
$$k_4 = hf(v_n + k_3) \qquad h = \Delta t \tag{25}$$

In general, the number and stability properties of fixed points with respect to the time step are roughly comparable to those of the second-order Runge–Kutta scheme. As an example, the stability diagram of Figure 3 (right), where $D_p = 4.62$ mm, can be compared with the second-order Runge–Kutta scheme. In general, the critical time step value, up to which the original fixed point is stable, is slightly larger in the fourth-order than in the second-order scheme. Also negative values of the bubble rise velocity are generated for large values of D_p, if the time step is not chosen small enough.

To summarize, Figure 4 shows the critical Δt in which the fixed point $v_*$of regime 4 in Eq. 10 becomes unstable for the different numerical schemes considered in this work: semianalytical scheme with fixed time step, Euler and Runge–Kutta of second and fourth orders. From them the most stable scheme is the fourth-order Runge–Kutta because it presents the highest critical Δt, but at the same time it is the most expensive with respect to the need of CPU time. The most unstable numerical schemes are the Euler and second-order Runge–Kutta, which provide nearly identical results for this case. This is because when the bubble velocity tends to the terminal velocity the second-order Runge–Kutta method tends to the Euler approach, as it can be readily seen from the Taylor series expansion of function f of Eq. 17 around the fixed-point v_*

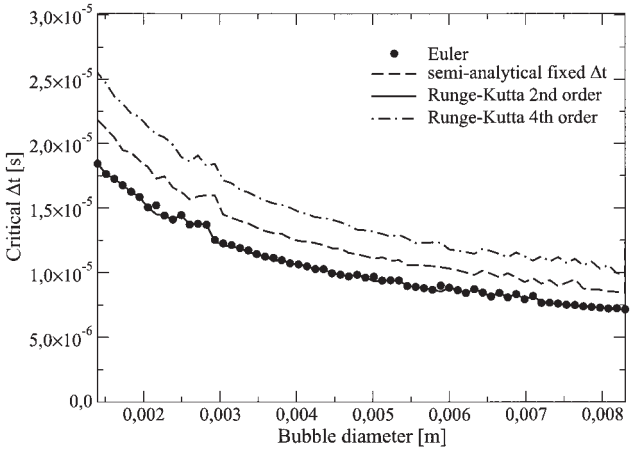

Figure 4. Critical time step for instability of the fixed point in regime 4 for the bubble drag law (Eq. 10) for the different numerical schemes used.

Finally, let us remember that if $K_m \neq 0$, the critical time step must be divided by $1 + K_m\rho/\rho_p$.

Settling of Heavy Solids in a Gas

Let us consider now the case of solids, with densities of the order 10^3 kg m^{-3}, settling under the action of gravity. Here, the following drag law has been used:

$$C_D = \begin{cases} \dfrac{24}{\mathrm{Re}}(1 + 0.173\,\mathrm{Re}^{0.657}) + \dfrac{0.413}{1 + 16{,}300\,\mathrm{Re}^{-1.09}} & \mathrm{Re} < 3.38 \times 10^5 \text{ (regime 1)} \\ 29.78 - 5.3\log_{10}\mathrm{Re} & 3.38 \times 10^5 < \mathrm{Re} < 4 \times 10^5 \text{ (regime 2)} \\ 0.1\log_{10}\mathrm{Re} - 0.49 & 4 \times 10^5 < \mathrm{Re} < 10^6 \text{ (regime 3)} \\ 0.19 - 8 \times 10^4\mathrm{Re}^{-1} & \mathrm{Re} > 10^6 \text{ (regime 4)} \end{cases} \tag{26}$$

Equation 26 was constructed by combining the Turton–Levenspiel[16] correlation (up to $\mathrm{Re} = 3.38 \times 10^5$) and the classical correlations for higher Reynolds numbers given by Clift et al.[12] Figure 5 shows both correlations, the recommended drag law of Clift et al. and that given by Eq. 26.

As previously explained, in this section, and opposite to the preceding one, velocities will be taken as positive in the direction of gravity (that is, downward). The steady states of the original differential Eq. 3 are again given by Eq. 4. It is possible to check that all fixed points of the differential equation are stable except in the *critical regime*, which corresponds to regime 2 of the drag correlation (Eq. 26) above. This physical instability is related to the transition from a laminar to a turbulent boundary layer around the particle leading to a path instability and therefore an oscillatory motion of the particle. Thus, three fixed points exist simultaneously for each Reynolds number in the range between $\mathrm{Re} \approx 1.5 \times 10^5$ and $\mathrm{Re} \approx 7 \times 10^5$. This Reynolds number regime is of practical interest for metereological balloons and large hailstones. Two of the three fixed points (the smallest and the largest ones) correspond to

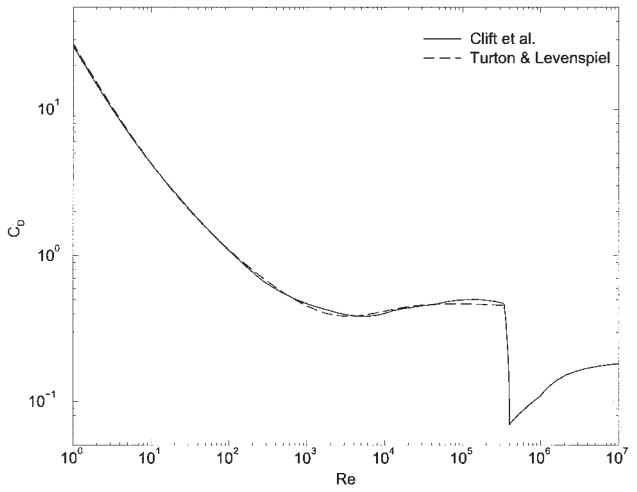

Figure 5. Standard drag correlations of Clift et al.[12] vs. the Turton–Levenspiel[16] correlation.

stable terminal settling velocities, whereas the third one connecting the upper and lower curves is unstable and thus cannot be reached experimentally. Which fixed point is reached in the critical regime depends on the initial conditions.

In the case of the semianalytical scheme, it is not difficult to realize that the fixed points of map 12 with the drag law (Eq. 26) coincide with the steady states of the differential Eq. 3. This time, however, restricting the time step of the semianalytical or Euler integration scheme to a fraction of the particle relaxation time results in a stable behavior of the fixed points in regimes 1, 3, and 4. Therefore, no artificial instabilities are created here. Of course, the unstable fixed point of the critical regime is also unstable in the numerical scheme. Nevertheless, from a mathematical perspective it is possible to see some numerical instabilities when the ratio $\Delta t/\tau_p$ grows above unity, but this possibility is not of practical interest. Therefore, the semianalytical approach is unconditionally stable in the case of heavy solids falling through a quiescent fluid, if the time step is simply chosen smaller than the relaxation time step. This allows one to choose a larger time step than that in the case of bubbles.

On the other hand, given that the Euler scheme is the most simple approximation to the numerical integration of functions, it is more unstable than the semianalytical approach. In spite of this, it is found that this simple scheme enjoys good stability properties provided that the time step is smaller than but still of the order of τ_p. Similarly to the case of bubbles, a bifurcation diagram and nonphysical values for the terminal velocity can be generated, if the time step becomes too large.

In the Runge–Kutta schemes, as in the previous ones, the fixed points of the original differential Eq. 3 remain stable for time steps lower than or equal to the relaxation time of the particle for both orders, second and fourth. However, as in the case of bubbles, *ghost* fixed points also appear for heavy solid particles. In addition, for sufficiently large values of the time step nonphysical (negative) values of the settling velocity are obtained.

Therefore, all the considered numerical schemes are well behaved in the case of heavy solids falling through a gas at rest.

Light Solid Spheres Rising in a Still Liquid

A particle whose density is smaller that that of the surrounding fluid will be called a "light particle." This kind of systems is relevant, for example, in ore treatment (flotation), biotechnology (inverse fluidized-bed bioreactors), or geophysics (rising meteorological balloons). Here the liquid will be taken as water. From the work of Karamanev and Nikolov[17] and Karamanev et al.[18] it is known that the free rise of a light spherical particle does not obey the laws of free settling for heavy particles, but is more similar to the behavior of a stiff bubble rising in a liquid. After extensive experimental work, using water as surrounding fluid and solids with different densities and diameters, Karamanev's group arrived at the following conclusions:

(1) For small enough Reynolds numbers, the terminal velocity of a light sphere can be described according to the standard drag curve.

(2) For large enough Reynolds numbers the drag coefficient is around 0.95.

(3) The particle density, at which the drag coefficient "jumps" from $C_D = 0.95$ to the standard drag curve, is different for different sphere diameters.

(4) The previous transition, taking place at a Reynolds number Re_{lim}, was always sharp, in a very narrow range of Re. Re_{lim} increased with increasing particle diameter.

It was found that the limiting Reynolds number was correlated with the particle diameter (written in meters) as

$$\mathrm{Re}_{lim} = 145{,}000 D_p \tag{27}$$

that is, the transition occurs always at a constant terminal velocity, independent of particle diameter or density, equal to 0.145 m/s when the solid rises in water at 20°C.

Therefore, the drag correlation for light solids can be expressed using the correlation given by Turton and Levenspiel[16] as

$$C_D = \begin{cases} \dfrac{24}{\mathrm{Re}}\left(1 + 0.173\,\mathrm{Re}^{0.657}\right) + \dfrac{0.413}{1 + 16{,}300\,\mathrm{Re}^{-1.09}} \\ \quad \mathrm{Re} < \mathrm{Re}_{\mathrm{lim}} \text{ (regime 1)} \\ 0.95 \\ \quad \mathrm{Re} > \mathrm{Re}_{\mathrm{lim}} \text{ (regime 2)} \end{cases} \tag{28}$$

Figure 6 shows this correlation for different particle diameters ($\rho_p = 400$ kg m^{-3}) together with the recommended drag law of Clift et al.[12] The transition between the standard drag and the fixed value of 0.95 is plotted as a step, following the experimental results. In practice, this is an ideal representation because in reality the existence of a smooth rapidly interpolating curve between both regimes is expected, but when used in numerical calculations, it can have unwarranted consequences.

It is necessary to point out the remarkable similarity between the drag correlation of clean bubbles rising in water and Eq. 28. Both consist of three parts: one decreasing monotonously, a second one increasing rapidly, and a third one being constant. This indicates that the dynamics of both systems must show similar behavior and, thus, the maps associated with the various numerical schemes for integrating Eq. 3 will present roughly the same nonlinear characteristics, which is indeed the case.

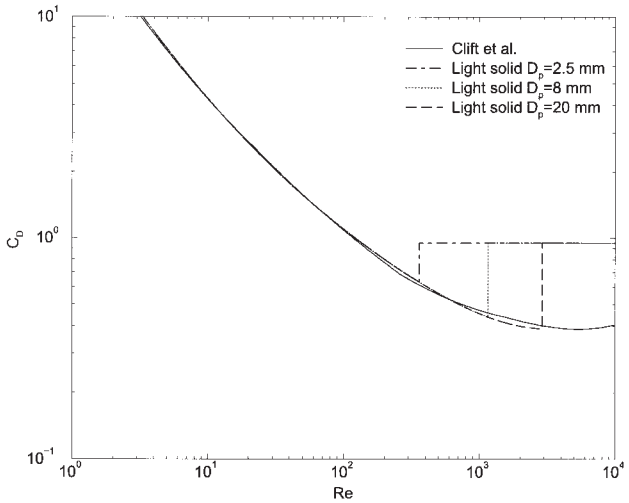

Figure 6. Drag correlation for light solids rising in water according to Eq. 28 for different particle diameters: $\rho_p = 400$ kg m^{-3}.

Therefore, the stability boundary of the semianalytical approach with time step adjusted to a fraction of the particle relaxation time will be given by a critical value for the parameter A (cf. Eq. 15), whose exact magnitude depends on the slope of the interpolating logarithmic straight line between regimes 1 and 2 in Eq. 28. For a step function, the stability of the intermediate fixed point of map 12 can be reached only in the limit $\Delta t \rightarrow 0$ corresponding to $A \rightarrow 1$.

For the stepwise, that is, discontinuous, interpolation, the other numerical schemes yield numerical stability of the fixed point corresponding to the terminal velocity of the transition between regimes 1 and 2 in the limit $\Delta t \rightarrow 0$ only. In the case of interpolating in a finite range of Reynolds numbers, the value of Δt ensuring stability of such intermediate fixed points will depend on the exact realization of the interpolation. Also, for the Runge–Kutta schemes stable "ghost" fixed points come into existence and for large time steps nonphysical negative values of the terminal velocity can be generated.

Conclusions

The investigation of the stability properties of the fixed points of the (Lagrangian) discretized particle motion equation have been presented in this article. It has been shown that iterating the maps induced by standard numerical schemes to solve the particle momentum equation may lead to artificial oscillations up to chaotic behavior in the time series of the particle velocity. It may even give rise to artificial steady states, that is, nonphysical terminal particle velocities. In the case of multiple stable steady states it depends on the initial conditions which one would eventually be reached. Each numerical method has its own critical parameter or time step value, which may be too small for practical purposes. The performance of the schemes depends strongly on the form of the drag coefficient. Additionally, it has been shown that rising bubbles and light solids in a surrounding fluid share the same nonlinear dynamics according to the similarity of the form of their drag laws. In the case of heavy solids falling through a fluid at rest, all the numerical integration schemes of the particle motion equation perform well enough, provided that the time step is smaller that the relaxation time of the particle. Overall, however, the semianalytical approach used in the engineering literature, with the time step adapted to the particle relaxation time, gives the best results because it represents the most direct, least time-consuming, and most stable iteration scheme out of the schemes investigated herein. Finally, precise criteria have been provided for optimizing the performance of the schemes keeping numerical stability.

Acknowledgments

The financial support of the Vicerrectoría de Investigaciones of the Universidad Autónoma de Occidente through the project "Simulación de Grandes Escalas aplicada al Flujo en Reactores de Columna de Burbujas" under reference number 03-PIM-09 is gratefully acknowledged.

Literature Cited

1. Crowe CT, Sommerfeld M, Tsuji Y. *Multiphase Flows with Droplets and Particles*. Boca Raton, FL: CRC Press; 1998.
2. Shirolkar JS, Coimbra CFM, Queiroz McQuay M. Fundamental aspects of modeling turbulent particle dispersion in dilute flow. *Prog Energy Combust Sci.* 1996;22:363-399.
3. Gouesbet G, Berlemont A. Eulerian and Lagrangian approaches for predicting the behavior of discrete particles in turbulent flows. *Prog Energy Combust Sci.* 1999;25:133-159.
4. Huber N, Sommerfeld M. Modelling and numerical calculation of dilute-phase pneumatic conveying in pipe systems. *Powder Technol.* 1998;99:90-101.
5. Ishii M. *Thermo-fluid Dynamic Theory of Two-Phase Flow*. Paris, France: Eyrolles; 1975.
6. Reeks MW. On the constitutive relations for dispersed particles in nonuniform flows. I: Dispersion in a simple shear flow. *Phys Fluids A.* 1993;5:750-761.
7. Zaichik LI. Modelling of the motion of particles in nonuniform turbulent flows using the equation for the probability density function. *J Appl Math Mech.* 1997;61:127-133.
8. Sommerfeld M, Kohnen G, Rüger M. Some open questions and inconsistencies of Lagrangian particle dispersion models. Proc of Ninth Symp on Turbulent Shear Flows, Paper 15-1; 1993.
9. Laín S, Göz MF. Instabilities in numerical simulations of dispersed two-phase flow. *Mech Res Commun.* 2000;27:475-483.
10. Maxey MR, Riley JJ. Equation of motion for a small rigid sphere in a nonuniform flow. *Phys Fluids.* 1983;26:883-889.
11. Magnaudet J. The forces acting on bubbles and rigid particles. Proc of ASME Fluids Eng. Div. Summer Meeting, Paper FEDSM97-3522; 1997.
12. Clift R, Grace JR, Weber ME. *Bubbles, Drops, and Particles*. New York, NY: Academic Press; 1978.
13. Tomiyama A. Struggle with computational bubble dynamics. Proc of the 3rd Int. Conf. on Multiphase Flow, Lyon, France, Jun. 8–12; 1998.
14. Laín S, Bröder D, Sommerfeld M. Experimental and numerical studies of the hydrodynamics in a bubble column. *Chem Eng Sci.* 1999;54:4913-4920.
15. Cartwright JHE, Piro O. The dynamics of Runge–Kutta methods. *Int J Bifurc Chaos.* 1992;2:427-449.
16. Turton R, Levenspiel O. A short note on the drag correlation for spheres. *Powder Technol.* 1986;47:83-86.
17. Karamanev DG, Nikolov LN. Free rising spheres do not obey Newton's law for free settling. *AIChE J.* 1992;38:1843-1846.
18. Karamanev DG, Chavarie C, Mayer RC. Dynamics of the free rise of a light solid sphere in liquid. *AIChE J.* 1996;42:1789-1792.

Manuscript received July 25, 2003, and revision received July 21, 2005.